Acta Geochim (2025) 44:1328–1339
https://doi.org/10.1007/s11631-025-00795-6

ORIGINAL ARTICLE

Geochemical fingerprints of apatite from the Qiongjiagang pegmatite-type lithium deposit, Himalaya

Xiao-Yan Jiang[1] · Qiang Fu[1,2] · Jiehua Yang[1] · Qiang Zhang[3] · Jinfeng Wang[4] · Haoze Yang[1,2] · Zongyong Yang[1] · Longgang Gao[1]

Received: 7 March 2025 / Revised: 30 April 2025 / Accepted: 27 May 2025 / Published online: 16 July 2025

Abstract Lithium is a critical strategic metal with significant reserves in pegmatites, serving as the primary source for global Li production. Apatite has attracted increasing attention as an indicator in petrogenesis studies and for the exploration of ore deposits. In this study, we investigated the volatile compositions and major and trace elements of apatite from the Qiongjiagang pegmatite-type lithium deposit in Himalaya. Apatite derived from spodumene pegmatite exhibits relatively constant and high total rare earth element (ΣREE+Y) concentrations, ranging from 5899 to 8540 ppm. In contrast, apatite in barren pegmatite displays evidently lower (ΣREE+Y) concentrations, varying between 1345 and 3095 ppm. The REE patterns of apatite in spodumene pegmatite generally exhibit a flat shape [$(La/Yb)_N = 1.55–2.15$)], with distinctively negative Eu anomalies ($Eu_N/Eu_N^* = 0.14–0.22$), slightly positive Ce anomalies ($Ce_N/Ce_N^* = 1.03–1.13$), and low Y/Ho ratios (28–30). By contrast, apatite in barren pegmatite shows middle rare earth element (MREE)-depleted downward-convex patterns [$(La/Yb)_N = 1.99–20.4$)], strongly negative Eu anomalies ($Eu_N/Eu_N^* = 0.01–0.14$), slightly positive Ce anomalies ($Ce_N/Ce_N^* = 1.10–1.24$), and high Y/Ho ratios (30–55, with an average of 50). Overall, the high concentrations of ΣREE (and Y) and low Th/U and Y/Ho ratios can serve as diagnostic indicators to distinguish apatite in spodumene pegmatite from that in barren pegmatite. Furthermore, the flat REE pattern may represent a common feature of apatite from lithium deposits. Differences in the Ce and Eu anomalies between apatite from these two kinds of pegmatites likely reflect formation under different redox conditions. Consequently, based on calculations derived from apatite volatile compositions, the melt associated with spodumene pegmatite may contain higher water content compared to that of the barren one. Therefore, the mineralized pegmatite system may incorporate substantial amounts of H_2O-rich fluids, which play a crucial role in lithium mineralization.

Keywords Apatite · Geochemical compositions · Pegmatite · Lithium deposit · Qiongjiagang

Supplementary Information The online version contains supplementary material available at https://doi.org/10.1007/s11631-025-00795-6.

✉ Xiao-Yan Jiang
jiangxiaoyan@mail.gyig.ac.cn

[1] State Key Laboratory of Critical Mineral Research and Exploration, Institute of Geochemistry, Chinese Academy of Sciences, Guiyang 550081, People's Republic of China

[2] College of Earth and Planetary Sciences, University of Chinese Academy of Sciences, Beijing 100049, People's Republic of China

[3] School of Earth and Planetary Sciences, Chengdu University of Technology, Chengdu 610059, Sichuan, People's Republic of China

[4] School of Resources, Environment and Safety Engineering, University of South China, Hengyang 421001, People's Republic of China

1 Introduction

Lithium (Li) is a critical metal of increasing economic significance. It has been utilized in a diverse array of industries, including nuclear applications, medicine, and renewable energy (Bibienne et al. 2020; Xu et al. 2023). Although Li is relatively enriched in the upper continental crust, with average concentrations of approximately 24 ppm (Rudnick and Gao 2003), its economic extraction requires extreme geological enrichment processes. Pegmatite-type Li

deposits, considered one of the most important economic sources for lithium, host rare minerals such as spodumene and petalite and reach high weight percent levels (Kesler et al. 2024). Pegmatites belong to highly fractionated granitic systems that experience complex magmatic evolution processes, including fractional crystallization, fluid saturation, and melt-fluid interaction (Linnen et al. 2012; London 2014, 2018). Whole-rock composition, traditionally used to trace fractional crystallization and crustal contamination, is susceptible to alterations and modifications of their original composition during subsequent geological processes. In light of the economic importance of highly evolved magmatic systems, an increasing number of studies have employed textures and composition of accessory minerals to trace their evolution.

Apatite is a ubiquitous calcium phosphate in granites and pegmatites (Pan and Fleet 2002; Webster and Piccoli 2015), as well as in various magmatic and hydrothermal ore deposits (Mao et al. 2016; Qu et al. 2021). Owing to its structural characteristics, apatite accommodates volatile substances and a wide range of trace elements, preserving the chemical signatures of its parent magma and changes of the crystallization environment in magmatic–hydrothermal systems (Sha and Chappell 1999; Pan and Fleet 2002; Jiang et al. 2020; Cao et al. 2021; Pan et al. 2021; Qu et al. 2021; Shi et al. 2024). Furthermore, the geochemical variations observed in apatite are highly sensitive to metallogenic processes and can be used to distinguish the fertile and barren igneous rocks (Pan et al. 2016; Zhang et al. 2023). Therefore, apatite has gained increasing attention as a critical petrogenetic indicator mineral, systematically employed to decode magma-fluid evolution and ore-forming processes due to its capacity to record multistage geochemical fingerprints.

The Qiongjiagang (QJG) pegmatite-type Li deposit, located in the Mount Qomolangma region within the Higher Himalayan leucogranite belt (Fig. 1). It has been recently discovered and represents the first economically significant pegmatite-type Li deposit identified in the Himalayas (Fig. 1b; Qin et al. 2021; Zhao et al. 2021). The geochemical compositions and textural attributes of apatite within the QJG pegmatite hold the potential to provide profound insights into the formative mechanisms of the Li ore deposit. Additionally, characterizing apatite in terms of its texture and geochemical compositions can help elucidate the nature of the parental magma, specifically parameters such as oxygen fugacity (f_{O2}) and H_2O. In this study, we investigated the major and trace element compositions of apatite from the QJG pegmatite-type Li deposit to characterize the nature of the magmas (e.g., f_{O2}, H_2O), compare the geochemical differences in apatite from ore-bearing and barren pegmatite, and evaluate a series of discrimination diagrams that may be useful for apatite as an indicator mineral in the exploration of pegmatite-type Li deposit.

2 Geological background

From north to south, the Himalayan orogenic belt consists of the Tethys Himalaya, the Higher Himalaya, and the Lower Himalaya (Fig. 1). The belt is characterized by extensive leucogranite, predominantly comprising two-mica granite, tourmaline granite, and garnet granite (Guillot and Le Fort 1995; Wu et al. 2020). These leucogranites are spatially widespread in the Tethys Himalaya and the Higher Himalaya, parallel to the extensional direction of the regional detachment system (Fig. 1b; Le Fort et al. 1987; Searle et al. 2009; Liu et al. 2024). The pegmatites are mainly distributed

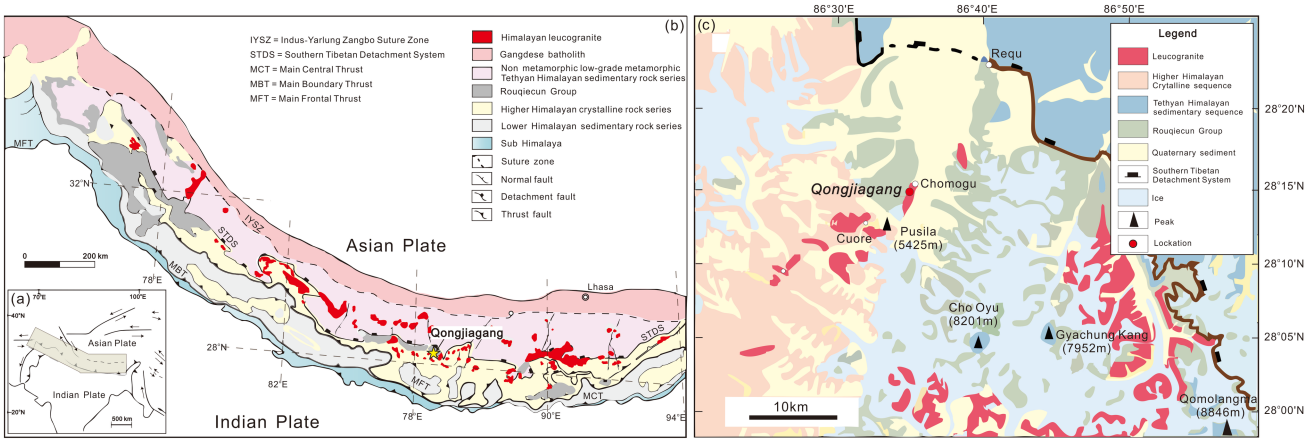

Fig. 1 **a** Simplified map of the Himalayan–Tibetan orogeny. **b** Simplified tectonic map showing the location of QJG pegmatite-type Li deposit in the Mount Qomolangma region and the distribution of Himalayan leucogranite in the Tethys Himalaya and the Higher Himalaya tectonic units (modified after Wu et al. 2020). **c** Schematic geological map of QJG and adjacent areas (modified after from Wu et al. 2020 and Qin et al. 2021), showing the distribution of pegmatite-type Li deposits

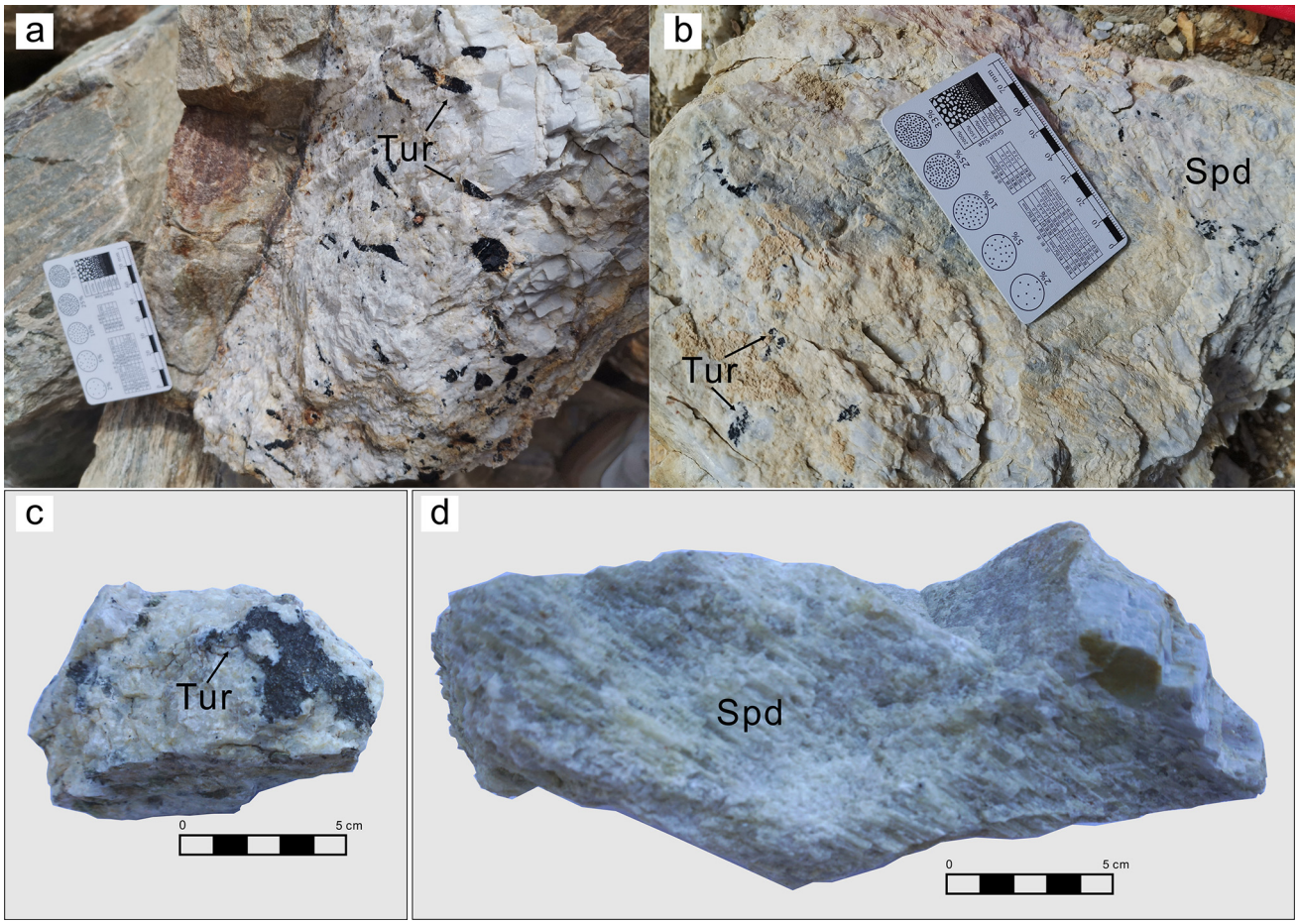

Fig. 2 **a** Outcrop of muscovite tourmaline pegmatite. **b** Outcrop of spodumene pegmatite. **c** Representative hand specimen of muscovite tourmaline pegmatite. **d** Representative hand specimen of spodumene pegmatite. Abbreviations: Tur = tourmaline, Spd = spodumene

around the leucogranites in domes or metamorphic rock formations (Wang et al. 2017), or as lenses/vesicles independently occurring within country rocks (Liu et al. 2020). In general, most of the Himalayan pegmatites exhibit simple zoning. Notably, a fraction of the pegmatites are associated with Be–Nb–Ta(W–Sn) rare-metal mineralization.

The recently discovered QJG pegmatite-type Li deposit is located in the Higher Himalayan leucogranite belt along the southern Tibetan detachment system beneath the Himalayan metamorphic rocks (Fig. 1b, c), and represents the first economically significant lithium resource of this genetic type in the Himalayan orogenic belt (Fig. 1; Qin et al. 2021; Zhao et al. 2021). Regional leucogranite bodies are dominated by tourmaline muscovite granite (Zhao et al. 2021), with associated pegmatites occurring as veins cross-cutting leucogranite bodies or as gradational facies transitions. Exploration in QJG has revealed approximately 40 spodumene pegmatite veins hosted within marble and schist units of the Rouqiecun Group. These veins vary in width, with the widest one exceeding 100 m (Zhao et al. 2021). Spodumene pegmatites from the QJG pegmatite-type Li deposit display limited internal zonation. In addition to spodumene pegmatites, there are also some barren pegmatites, which form isolated bodies and do not intersect with spodumene pegmatites (Qin et al. 2021; Zhao et al. 2021; Liu et al. 2024; Shi et al. 2024).

This study focuses on two types of pegmatites, i.e., barren pegmatite (muscovite tourmaline pegmatite) and spodumene pegmatite. Barren pegmatite exhibits a mineral assemblage dominated by feldspar and quartz, with subordinate tourmaline and muscovite, accompanied by accessory minerals apatite and zircon (Figs. 2, 3). Spodumene pegmatite contains the ore mineral spodumene, with minor amounts of columbite and cassiterite, and gangue minerals including microcline, albite, quartz, tourmaline, and garnet (Figs. 2, 3). Accessory phases include apatite, zircon, and monazite.

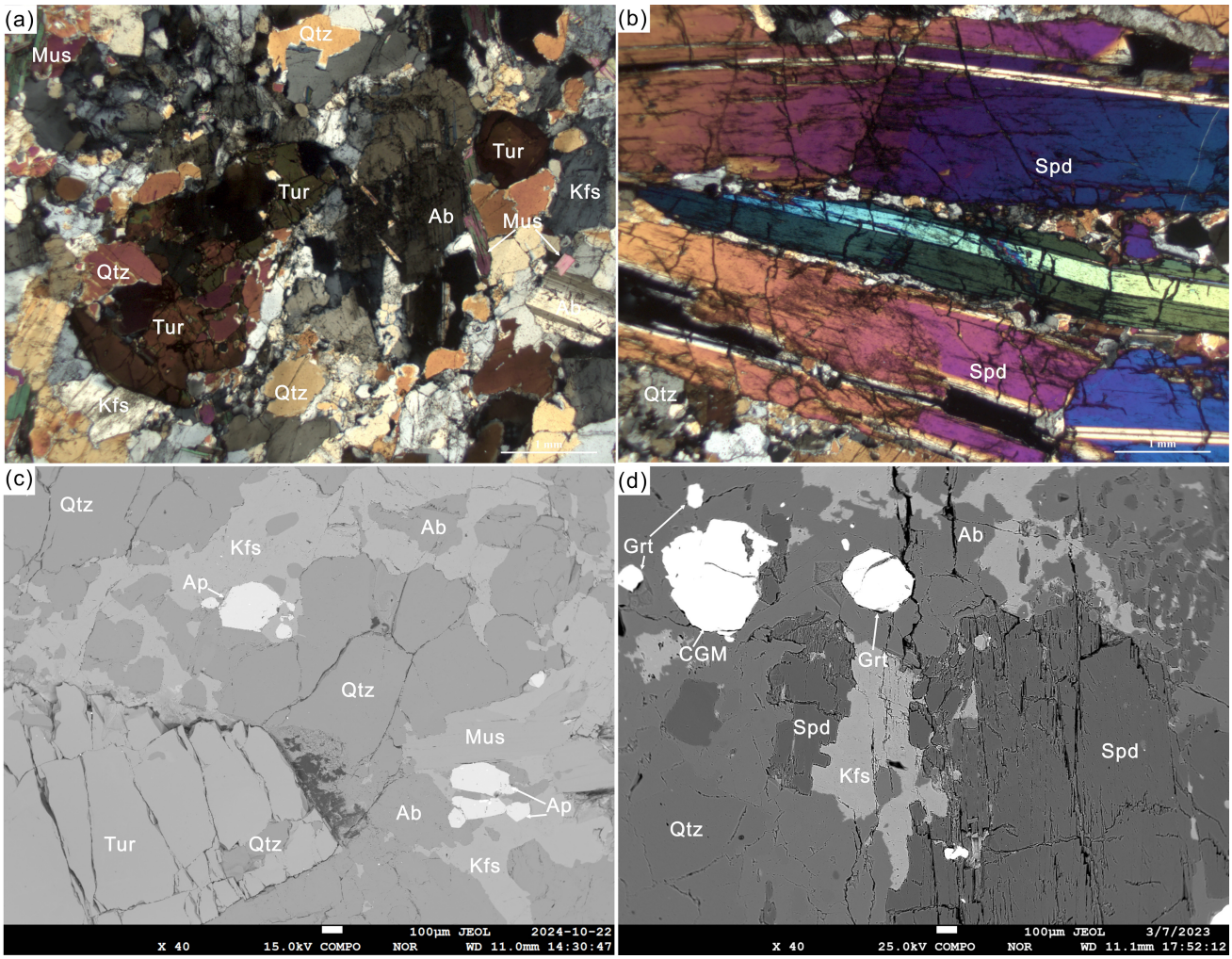

Fig. 3 **a** and **b** Photomicrographs of muscovite tourmaline pegmatite and spodumene pegmatite, respectively. Twins in plagioclase. Dark brown and green tourmaline grains. **c** and **d** Backscatter electron (BSE) images of muscovite tourmaline pegmatite and spodumene pegmatite, respectively. Abbreviations: Tur. tourmaline, Spd. spodumene, Qtz. quartz, Ab. albite, Kfs. K-feldspar, Ap. apatite, Grt. garnet

3 Analytical method

Apatite grains analyzed in this study were obtained from bulk rock samples using conventional rock crushing, followed by separation via heavy liquids and magnetic susceptibility-based partitioning. Representative grains were mounted in epoxy resin and polished to expose interior grain sections for subsequent analysis. Transmitted/reflective and cathodoluminescence (CL) and BSE images were taken by microscope (Leica DM2700P) and field-emission scanning electron microscope (SEM; JEOL JSM-7800F) coupled to a CL detector, respectively, to reveal internal texture and inclusions or cracks. These images were taken at the State Key Laboratory of Critical Mineral Research and Exploration (SKLCMRE), Institute of Geochemistry, Chinese Academy of Sciences (IGCAS).

Major element compositions of apatite were determined using a JEOL JXA-8100 electron microprobe at the SKLCMRE, IGCAS. The microprobe operated at an accelerating voltage of 25 kV, a beam current of 10 nA, and a beam spot diameter of 10 μm. A counting time of 20 s was used for most elements, with 40 s for F and 10 s for P and Ca. Standardization employed norbergite for fluorine (F), $Ba_5(PO_4)_3Cl$ for chlorine (Cl), and apatite for calcium (Ca) and phosphorus (P). Fluorine Kα and Cl were analyzed using LDE1 PET crystals, respectively. Data correction was achieved using the JEOL internal ZAF correction model. Analytical precision for most major elements exceeded 1%, whereas measurements of F and Cl exhibited lower precision (~5%).

In situ trace element compositions of apatite were determined using laser ablation–inductively coupled plasma–mass spectrometry (LA-ICP-MS) at the SKLCMRE, IGCAS, with an Agilent 7900 ICP-MS equipped

with a GeoLasPro 193 nm ArF excimer laser ablation system. Each spot analysis began with a 20 s background measurement followed by 40 s sample data acquisition with the laser switched on, using a laser repetition rate of 10 Hz and a beam of ~30 μm. All reference materials were analyzed at the beginning of each session and after every 10 unknowns using the same conditions as for the samples. Calcium (Ca) was selected as the internal standard for calibrating concentrations of other elements. Durango and NIST SRM 612 were employed as quality control samples. Offline data processing was performed using ICPMSDataCal software (Liu et al. 2010). The analytical accuracy was better than 10% for most trace elements.

The major and trace element data for apatite are reported in Tables S1 and S2.

4 Results

4.1 Apatite texture

Apatite crystals from both spodumene pegmatite and barren pegmatite predominantly show two types of textures. Most of apatite crystals are euhedral to subhedral prismatic, manifest transparency under transmitted light conditions and present gray to dark and homogeneous areas in CL images. These crystals contain scarce inclusions (Fig. 4). Some apatite crystals show narrow and bright overgrowth rims or dark intersecting veins (Fig. 4). Inclusions are observed to occur in isolation, in clustered aggregations, or randomly distributed throughout certain grains. This distribution pattern indicates the potential occurrence of late-stage magmatic-hydrothermal processes.

4.2 Apatite major element composition

All the analyzed apatite crystals are fluorapatite, with F content ranging from 2.78 to 4.50 wt.% and extremely low Cl content (below 0.1 wt.%, Table S1 and Fig. 5). Notably, certain apatite crystals exhibited F content that surpassed the theoretically predicted maximum F content for apatite, which is 3.77 wt.%. Apatite from barren pegmatite has relatively lower F (2.78–3.74 wt.%) content and higher Cl content (up to 0.37 wt.%) in contrast to apatite from spodumene pegmatite, which has F content ranging from 3.00 to 3.71 wt.% and Cl content of no more than 0.01 wt.% (Fig. 5c). Both types of apatite show similarly low SO_3 content, falling below the detection limit up to a maximum of 0.02 wt.% (Fig. 5b). The calculated OH values, based on F and Cl content, reveal a relatively broader range of OH in apatite from barren pegmatite (0.01–0.52 wt.%) than that from spodumene pegmatite (0.11–0.39 wt.%) (Fig. 5d).

4.3 Apatite trace element composition

The chondrite-normalized REE patterns of apatite reveal fundamental compositional contrasts between barren and spodumene pegmatites (Fig. 6a). Apatite grains in spodumene pegmatite have relatively constant and elevated total rare earth (ΣREE+Y) concentrations in the range of 5899–8540 ppm, generally present in relatively flat and weakly fractionated patterns. The $(La/Yb)_N$ ratios range from 1.55 to 2.15, with pronounced negative Eu anomalies ($Eu_N/Eu_N^* = 0.14–0.22$) and slightly positive Ce anomalies ($Ce_N/Ce_N^* = 1.03–1.13$). Light rare earth element (LREE)/heavy rare earth element (HREE) ratios are clustered around 2, and the Y/Ho ratios vary in the range of 28–30 (averaging 29) (Fig. 6a, b). The Sr and Y concentrations of apatite (Sr = 129–147 ppm, Y = 2370–5571 ppm) vary within a narrow range and present a slightly positive correlation (Figs. 6b, 7b).

In contrast, apatite grains in barren pegmatite have obviously low (ΣREE+Y) concentrations varying from 1345 to 3095 ppm, and display MREE-depleted convex

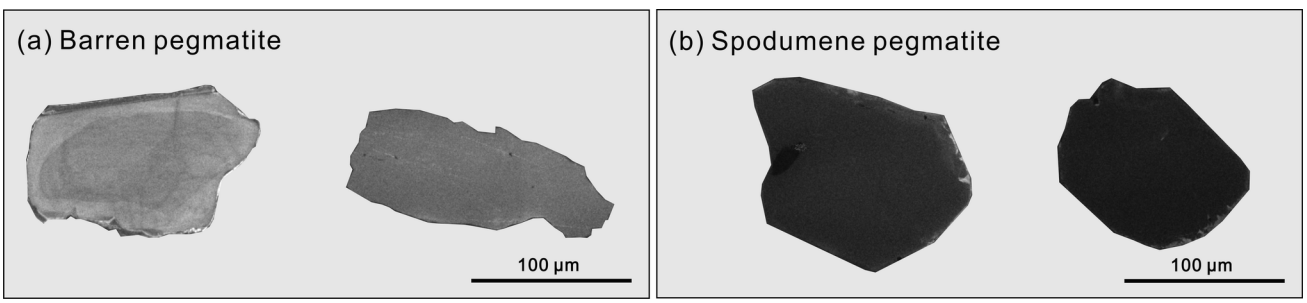

Fig. 4 Representative CL images of apatite from the QJG pegmatite-type Li deposit. **a** Apatite from barren pegmatite. **b** Apatite from spodumene pegmatite

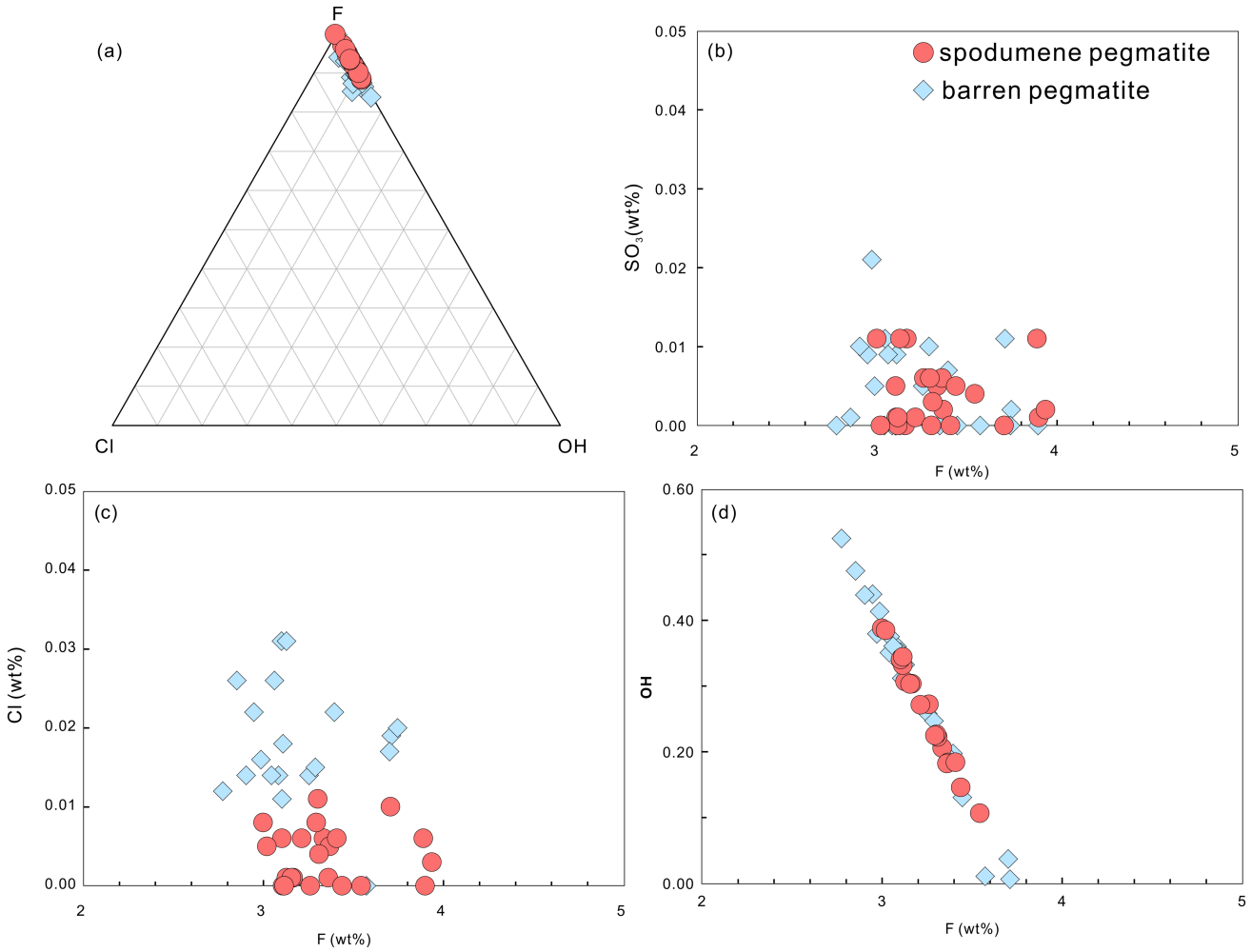

Fig. 5 Volatile element content of apatite from barren pegmatite and spodumene pegmatite. **a** Ternary diagram of F-Cl-OH. **b** F versus SO_3. **c** F versus Cl. **d** F versus OH

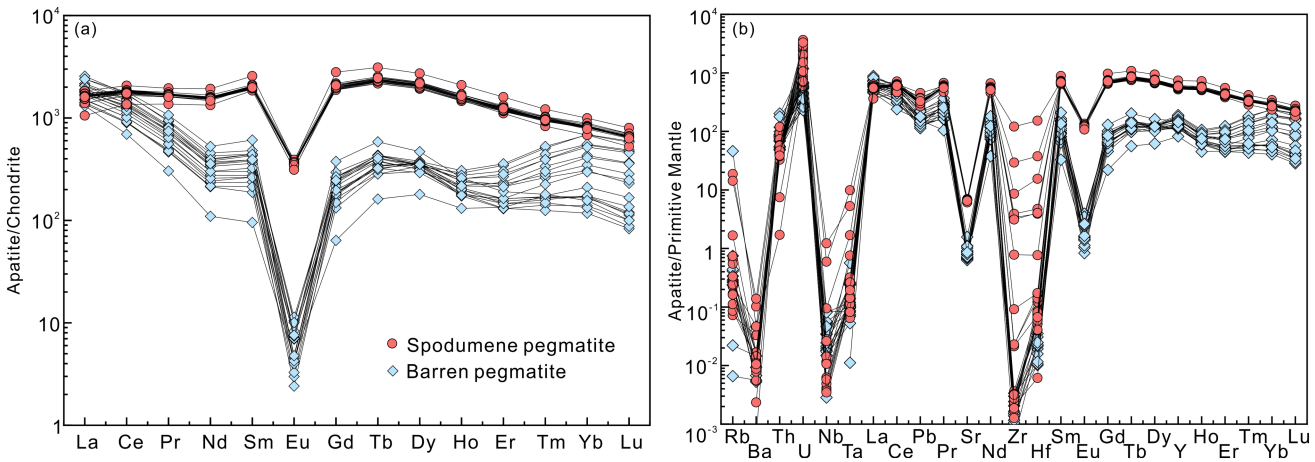

Fig. 6 **a** Chondrite-normalized REE patterns, and **b** primitive-mantle-normalized trace element patterns of apatite from the QJG pegmatite. Normalization values are from Sun and McDonough (1989)

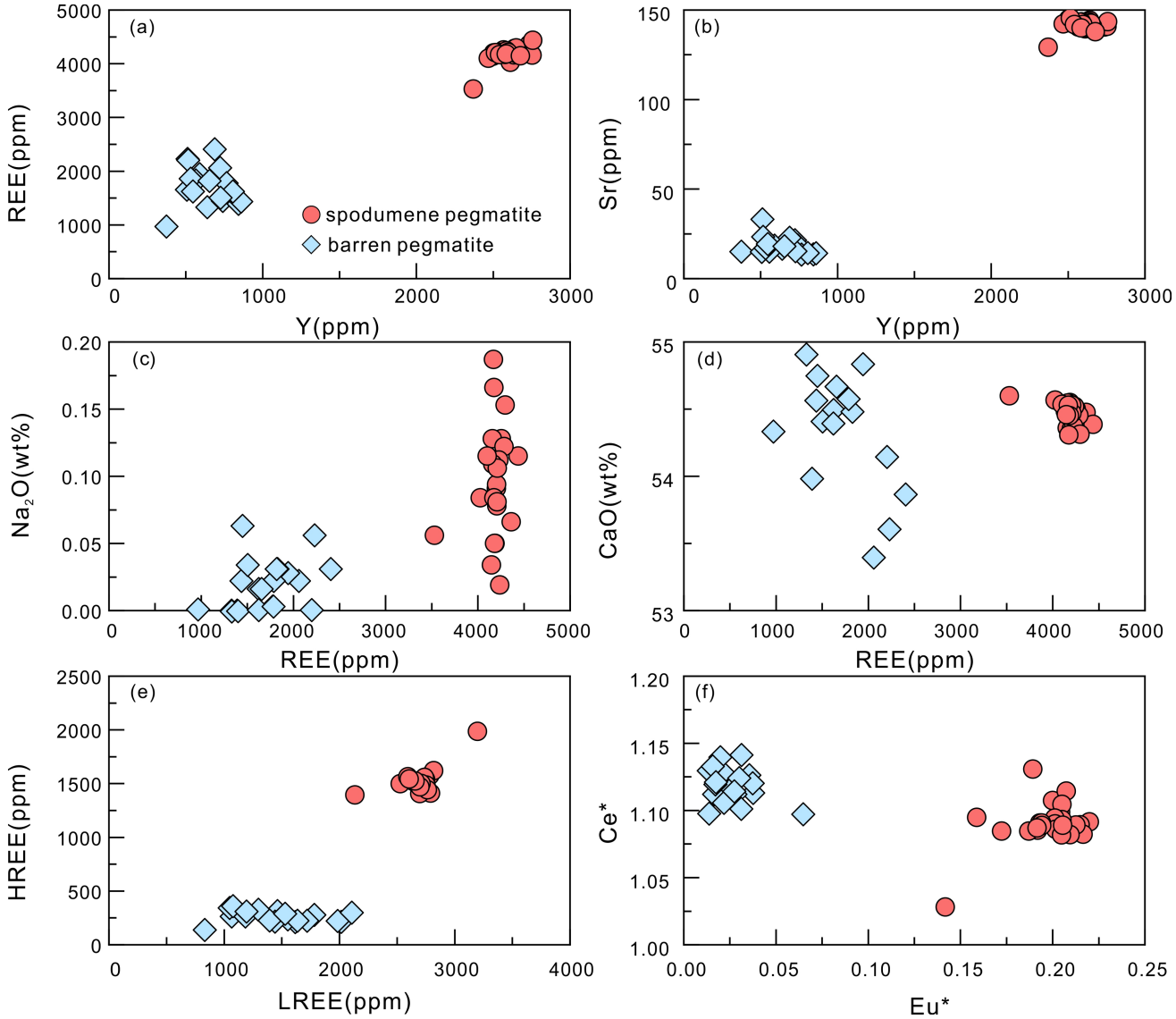

Fig. 7 Binary variation diagrams highlighting the contrasting composition of apatite from barren pegmatite and spodumene pegmatite in the QJG pegmatite-type Li deposit

downward REE patterns. They have varied $(La/Yb)_N$ ratios (1.99–20.4), strongly negative Eu anomalies ($Eu_N/Eu_N^* = 0.01–0.14$), and slightly positive Ce anomalies ($Ce_N/Ce_N^* = 1.10–1.24$). They exhibit a significant REE tetrad effect, as evidenced by $TE_{1,3}$ ratios varying from 1.09 to 1.20 (only one outlier with $TE_{1,3} = 0.8$). LREE/HREE ratios vary relatively widely from 3 to 8, and the Y/Ho ratios range from 30 to 55 (with an average of 50). They have relatively lower Sr and Y concentrations (Sr = 13.4–33.1 ppm, Y = 374–860 ppm) and show positive correlations (Fig. 7a).

5 Discussion

5.1 Magmatic or hydrothermal apatite?

The apatite grains in QJG pegmatites appear to have a predominantly magmatic origin rather than being directly derived from hydrothermal fluid, given the following considerations. Firstly, in CL images, magmatic apatite typically exhibits a homogeneous and bright appearance, devoid of mineral inclusions, contrasting with hydrothermal apatite that typically exhibits anhedral morphology and contains

inclusions of monazite and xenotime or overgrowth rims formed via coupled dissolution–reprecipitation processes (Harlov 2015). Secondly, magmatic apatite occurs as interstitial phases spatially associated with or encapsulated by primary K-feldspar and tourmaline (Fig. 3c), demonstrating textural equilibrium indicative of co-genetic crystallization from pegmatitic magma. Thirdly, although hydrothermal apatite may possess variable and low (ΣREE+Y) concentrations and could be challenging to differentiate from magmatic apatite that has undergone fluid interaction, magmatic apatite is systematically enriched in MREE (Webster and Piccoli 2015) and typically retains REE patterns resembling pristine magmatic composition even after alteration (Bouzari et al. 2016; Cao et al. 2021). In contrast, hydrothermal apatite exhibits distinct downward-convex REE patterns. Furthermore, hydrothermal apatite is markedly depleted in most trace elements relative to its magmatic counterpart, including REE, Y, Li, Na, Mg, K, Mn, Fe, and Ga, despite showing a broader (ΣREE+Y) concentration range (ranging from < 1 ppm to approximately 1500 ppm) (Qu et al. 2022; Zhang et al. 2023; Cao et al. 2024). In this study, apatite from both spodumene and barren pegmatites has relatively consistent and high (ΣREE+Y) concentrations and strongly negative Eu anomalies. Above all, this multiproxy diagnostic framework confirms crystallization of apatite in QJG pegmatite mainly from fractionated magmas.

While textural and geochemical evidence predominantly supports a magmatic origin, the potential influence of hydrothermal fluid cannot be categorically excluded. The apatite grains appear as bright rims, stringers, or heterogeneous domains that either replace or crosscut preexisting apatite grains (Fig. S1). Such features are typical of apatite formation resulting from the hydrothermal replacement of magmatic apatite (Xing and Wang 2017; Wang and Wang 2020). The comparatively lower total REE concentrations of apatite in barren pegmatite, relative to those in spodumene pegmatite, could potentially be ascribed to the leaching and mobilization of REE during hydrothermal activity (Williams-Jones et al. 2012; Li and Zhou 2015; Cao et al. 2024).

5.2 Estimation of magma oxidation state and water content

Apatite serves as a critical repository and geochemical modulator of redox-sensitive elements (such as Ce, Eu, and S), thereby functioning as a valuable petrogenetic indicator for deducing oxidation states of co-genetic magmas (Cao et al. 2012; Sha and Chappell 1999; Miles et al. 2014). Both Eu and Ce possess two ionic valences, namely Eu^{2+} and Eu^{3+}, and Ce^{3+} and Ce^{4+}. Given that the large ionic radius of Eu^{2+} (1.25 Å) ions precludes substitution in the Ca^{2+} (1.00 Å) lattice site, Eu^{3+} (0.947 Å) demonstrates favorable compatibility through substitution (Sha and Chappell 1999; Belousova et al. 2002). This crystallographically controlled fractionation generates markedly negative Eu anomalies during apatite precipitation. Apatite exhibiting a less distinct negative Eu anomaly might potentially signify crystallization from a relatively more oxidized magma (Belousova et al. 2002; Mercer et al. 2020).

Our analytical results reveal a systematic disparity in Eu partitioning between spodumene and barren pegmatites. Spodumene pegmatite exhibits substantially elevated Eu/Eu* ratios (0.14–0.22) compared to those in barren pegmatite (0.01–0.14) (Fig. 7f). This indicates that Eu in spodumene pegmatite is likely to occur as Eu^{3+} in a greater proportion than in barren pegmatite, implying crystallization from a relatively more oxidized magmatic source. Similarly, apatite demonstrates a significant preference for Ce^{3+} over Ce^{4+}. The lower Ce/Ce* ratio of apatite from spodumene pegmatite (1.03–1.13) compared to barren pegmatite (1.10–1.24) might also suggest that it is formed in a less reduced state (Fig. 7f). This integrated redox proxy approach demonstrates that Li mineralization in the studied pegmatites is most likely linked to a less reducing environment.

Although Eu anomalies in apatite offer insights into magmatic oxygen fugacity, their utility as redox proxies remains constrained by petrogenetic complexities, particularly those related to whole-rock systems such as bulk composition heterogeneity and plagioclase fractionation processes (Bromiley 2021). Previous works have revealed a general absence of significant Ce anomalies in most apatite specimens (Belousova et al. 2002; Chu et al. 2009). Analysis of spodumene pegmatites reveals limited Ce anomalies (Ce/Ce* = 1.03–1.13), potentially reflecting the influence of the magmatic fluids rather than primary magmatic signatures (Wu et al. 2025). Consequently, these geochemical signatures cannot provide definitive constraints on magmatic redox conditions but can at least prove that they formed under not completely the same redox states. Further analysis and evidence provided by other minerals and whole rock are needed to reflect primary oxygen fugacity signatures.

The H_2O content in magma, a significant physical–chemical parameter, can be approximately quantified via apatite chemistry. Li and Costa (2020) proposed a thermodynamic model using apatite volatiles (F, Cl, and OH) and exchange coefficients ($K_D^{OH\text{-}Cl}$, $K_D^{OH\text{-}F}$, $K_D^{Cl\text{-}F}$ pairs) to provide critical constraints on melt H_2O content. For QJG pegmatite apatite crystals of fluorapatite, the OH–F pair was adopted. Cationic abundance (Ca and P) and anion content (F and Cl) (normalized to atoms per formula unit) and mole fractions of F (x_F^{Ap}), Cl (x_{Cl}^{Ap}), and OH (x_{OH}^{Ap}) were determined by electron probe microanalysis (EPMA) data. The QJG intrusive system temperature (566–493 °C for spodumene pegmatite; 601–444 °C for barren pegmatite) was constrained according to the Ti-in-K-feldspar geothermometer calculated by Liu et al. (2024). As the calculator created by Li and Costa

(2020) requires melt temperature, which may be higher than feldspar crystallization, maximum values from this geothermometer are utilized. Magma F content was calculated via $F_{\mathrm{melt}}(\mathrm{wt.\%}) = x_{\mathrm{F}}^{\mathrm{Ap}} / x_{\mathrm{OH}}^{\mathrm{Ap}} * K_{(\mathrm{OH\text{-}F})}^{\mathrm{D}} * 6.18$ (Li and Hermann 2017). Calculations revealed that the parental magma of barren pegmatite had 2.8–4.4 wt.% H_2O, which is slightly below the upper crustal pressure melt saturation threshold (5–8 wt.%, Troch et al. 2022). The spodumene pegmatite melt had approximately 6.4–14.3 wt.% H_2O, exceeding the saturation limit. Although significant uncertainties (±30%–40%) accompany these estimates, the systematic contrast links Li enrichment to hydrous, volatile-saturated melts.

5.3 Differences in apatite composition between ore-bearing and ore-barren pegmatites

Previous studies have discussed the diverse mechanisms governing REE incorporation in apatite. The primary charge-compensating coupled substitutions facilitating the incorporation of REE into apatite are detailed as follows (Watson and Green 1981; Rønsbo 1989; Fleet and Pan 1995):

$$\mathrm{Na}^{+} + (\mathrm{Y} + \mathrm{REE})^{3+} = 2\mathrm{Ca}^{2+}; \quad (1)$$

$$\mathrm{Si}^{4+} + (\mathrm{Y} + \mathrm{REE})^{3+} = \mathrm{P}^{5+} + \mathrm{Ca}^{2+}. \quad (2)$$

In the study of apatite grains in barren pegmatite, a positive correlation between Na_2O and REE (Fig. 7c) and a roughly negative correlation between CaO and REE were observed (Fig. 7d). These trends imply that variations in REE and Y incorporation are predominantly governed by the coupled substitution mechanism of Eq. (1). In contrast, in apatite grains from spodumene pegmatite, REE concentrations remain constant despite variations in Na_2O and CaO (Fig. 7c, d), indicating that additional factors influence REE concentration fluctuations, such as the REE pattern and concentration of the host magma and the magmatic fractional crystallization.

In apatite from spodumene pegmatite, these parameters remain relatively constant, and no significant correlative relationship exists between them and variations in Li concentration (Fig. 8). Furthermore, the Li concentration in apatite from spodumene pegmatite (ranging from 24.1 to 93.3 ppm, with an average of 32.2 ppm) is markedly higher than that in barren pegmatite (ranging from 6.83 to 24.1 ppm, with an average of 15.9 ppm; Fig. 8). This difference is governed primarily by the compositional characteristics of the parent magma of the host rock. Therefore, in spodumene pegmatite, the Li concentration in apatite is predominantly controlled by the composition of the parent magma.

In magmatic systems, Li, Y, Sn, Sr, Mn, and REE are classified as incompatible elements. For barren pegmatite, the positive correlations observed between Li and REE, REE+Y, Sn, Sr, and MnO (Fig. 8) indicate that magmatic differentiation acts as an important enrichment mechanism. Apatite exhibits a pronounced affinity for concentrating REE, with a particular preference for Eu^{3+} relative to adjacent REE. The variability in REE patterns displayed by apatite from diverse rock types substantially reflects the REE signature of the parental magma, thereby highlighting the extent of prior melt evolution. The irregularity in the REE patterns of most apatite crystals from barren pegmatite can be attributed to the tetrad effect, which suggests that fluid–melt interaction occurs in the late magmatic-hydrothermal processes (Irber 1999). The variability in Li concentration seems like also influenced by late-stage fluid interaction, as indicated by the positive correlation tendency between Li and $TE_{1,3}$ (with values spanning from 1.1 to 1.2, except for a single outlier at 0.8; Fig. S2).

5.4 Implications for mineral exploration

Because of its capacity to incorporate a wide spectrum of elements within its crystal lattice, apatite has increasingly been recognized as a valuable geochemical indicator for petrogenetic studies and mineral exploration recognition (Sha and Chappell 1999; Bouzari et al. 2016; Mao et al. 2016; Cao et al. 2012, 2021, 2024; O'Sullivan et al. 2020; Pan et al. 2021; Zhang et al. 2023; Wu et al. 2024; Shi et al. 2024). In this study, our systematic analysis reveals that apatite grains in the spodumene pegmatite exhibit markedly elevated concentrations of REE, LREE, HREE, Y, Li, and Sr compared to those in barren pegmatites (Figs. 7, 8). These enrichments indicate that REE, Y, Li, and Sr were concentrated during the mineralization process. The high abundance of REE (and Y), combined with low Th/U and Y/Ho ratios, serves as diagnostic criteria for identifying Li-bearing pegmatites (Fig. 8). The characteristic flat REE pattern observed in apatite may represent a common geochemical feature associated with Li deposits. Furthermore, the inferred volatile content from apatite analysis implies that the melt in spodumene pegmatite likely contains higher H_2O content than that in barren pegmatite. Thus, the mineralized pegmatite system may host substantial quantities of H_2O-rich fluid, which plays a critical role in lithium mineralization. Therefore, apatite holds potential as an exploration tool for similar lithium deposits.

6 Conclusions

Systematic major and trace element analyses of apatite in QJG pegmatite highlight the utility of apatite geochemistry as a robust petrogenetic indicator for evaluating Li metallogenic potential. Firstly, based on the diagnostic texture

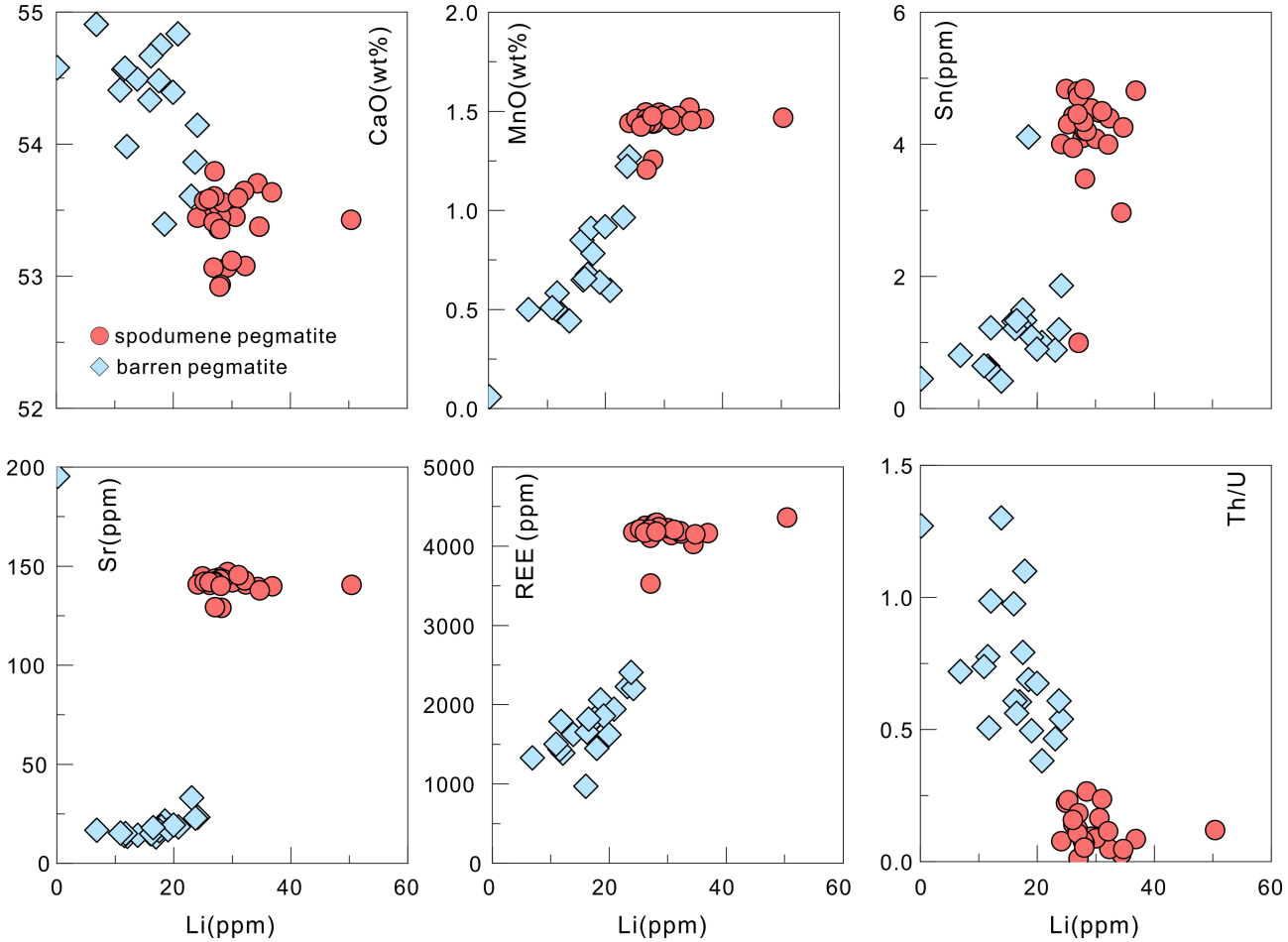

Fig. 8 Binary diagrams showing the compositional relationships between Li and other components in apatite from barren pegmatite and spodumene pegmatite in the QJG pegmatite-type Li deposit

characteristics and geochemical composition, apatite grains from QJG pegmatite are predominantly of magmatic origin. However, certain textural and compositional variations imply the existence of late-stage melt–fluid interaction. Secondly, the redox-sensitive elements (Eu and Ce) of the apatite indicate different crystallized redox states between the spodumene pegmatite and barren pegmatite. Thirdly, the calculations based on volatiles of apatite suggest that the magma of spodumene pegmatite had attained more H_2O content than that of barren pegmatite, which is likely a necessary factor for Li enrichment. Finally, the REE characteristics and the correlations between elements (e.g., Li, Sr, Y) of apatite provide geochemical criteria for lithium exploration targeting. Above all, apatite can be used as a key petrogenetic indicator mineral for Li mineralization systems.

Acknowledgements This work was funded by the Major Research Plan of the National Natural Science Foundation of China (92162323), Strategic Priority Research Program of the Chinese Academy of Sciences (XDA0430101), and Guizhou Provincial Science and Technology Projects No. ZK[2023]052. We thank Xiang Li, Yun Li and Shaohua Dong for CL images and EPMA analysis, Yanwen Tang and Junjie Han for LA-ICPMS analysis, and Dr. Xiaochi Liu for help in the field.

Author contributions Xiao-Yan Jiang: conceptualization, methodology, writing—original draft, writing—review and editing, formal analysis, funding acquisition; Qiang Fu: resources; Jiehua Yang: supervision, project administration; Qiang Zhang: data curation; Jinfeng Wang: investigation; Haoze Yang: visualization; Zongyong Yang: resources; Longgang Gao: resources.

Declarations

Conflict of interest The authors declare that they have no conflict of interest.

References

Belousova EA, Griffin WL, O'Reilly SY, Fisher NI (2002) Apatite as an indicatormineral for mineral exploration: trace-element

composition and their relationship to host rock type. J Geochem Explor 76:45–69

Bibienne T, Magnan JF, Rupp A, Laroche N (2020) From mine to mind and mobiles: society's increasing dependence on lithium. Elements 16(4):265–270. https://doi.org/10.2138/gselements.16.4.265

Bouzari F, Hart CJR, Bissig T, Barker S (2016) Hydrothermal alteration revealed by apatite luminescence and chemistry: a potential indicator mineral for exploring covered porphyry copper deposits. Econ Geol 111(6):1397–1410. https://doi.org/10.2113/econgeo.111.6.1397

Bromiley GD (2021) Do concentrations of Mn, Eu and Ce in apatite reliably record oxygen fugacity in magmas? Lithos 384:105900. https://doi.org/10.1016/j.lithos.2020.105900

Cao MJ, Li GM, Qin KZ, Seitmuratova EY, Liu YS (2012) Major and trace element characteristics of apatites in granitoids from central Kazakhstan: implications for petrogenesis and mineralization. Resour Geol 62(1):63–83. https://doi.org/10.1111/j.1751-3928.2011.00180.x

Cao MJ, Evans NJ, Hollings P, Cooke DR, McInnes BI, Qin KZ (2021) Apatite texture, composition, and O-Sr-Nd isotope signatures record magmatic and hydrothermal fluid characteristics at the black mountain porphyry deposit, Philippines. Econ Geol 116(5):1189–1207. https://doi.org/10.5382/econgeo.4827

Cao YH, Zhou LQ, Brzozowski M, Wang CY (2024) Apatite and pyroxene as records of magmatic–hydrothermal processes and platinum-group mineral (PGM) formation in the Wengeqi mafic–ultramafic intrusion, Inner Mongolia, China: the role of oxidized, H_2O-rich magmas. Chem Geol 670:122359. https://doi.org/10.1016/j.chemgeo.2024.122359

Chu MF, Wang KL, Griffin W, Chung SL, O'Reilly SY, Pearson NJ, Iizuka Y (2009) Apatite Composition: Tracing Petrogenetic Processes in Transhimalayan Granitoids. J Petrology 50(10):1829–1855. https://doi.org/10.1093/petrology/egp054

Fleet ME, Pan YM (1995) Crystal chemistry of rare earth elements in fluorapatite and some calc-silicates. EJM 7(3):591–606. https://doi.org/10.1127/ejm/7/3/0591

Guillot S, Le Fort P (1995) Geochemical constraints on the bimodal origin of High Himalayan leucogranites. Lithos 35(3–4):221–234. https://doi.org/10.1016/0024-4937(94)00052-4

Harlov DE (2015) Apatite: a fingerprint for metasomatic processes. Elements 11(3):171–176. https://doi.org/10.2113/gselements.11.3.171

Irber W (1999) The lanthanide tetrad effect and its correlation with K/Rb, Eu/Eu, Sr/Eu, Y/Ho, and Zr/Hf of evolving peraluminous granite suites. Geochim Cosmochim Acta 63(3–4):489–508. https://doi.org/10.1016/S0016-7037(99)00027-7

Jiang XY, Deng JH, Luo JC, Zhang LP, Luo ZB, Yan HB, Sun WD (2020) Petrogenesis of early cretaceous adakites in tongguanshan Cu–Au polymetallic deposit, Tongling region. Eastern China Ore Geol Rev 126:103717. https://doi.org/10.1016/j.oregeorev.2020.103717

Kesler S, Gruber P, Medina P, Keoleian G, Everson M, Wallington T (2024) Global lithium resources: relative importance of pegmatite, brine and other deposits. Ore Geol Rev 48(5):55–69

Le Fort P, Cuney M, Deniel C, France-Lanord C, Sheppard SMF, Upreti BN, Vidal P (1987) Crustal generation of the Himalayan leucogranites. Tectonophysics 134(1–3):39–57. https://doi.org/10.1016/0040-1951(87)90248-4

Li XC, Zhou MF (2015) Multiple stages of hydrothermal REE remobilization recorded in fluorapatite in the Paleoproterozoic Yinachang Fe–Cu–(REE) deposit, Southwest China. Geochim Cosmochim Acta 166:53–73. https://doi.org/10.1016/j.gca.2015.06.008

Li WR and Costa F (2020) A thermodynamic model for F-Cl-OH partitioning between silicate melts and apatite including non-ideal mixing with application to constraining melt volatile budgets. Geochim Cosmochim Acta 269:203–222. https://doi.org/10.1016/j.gca.2019.10.035

Li H. and Hermann J. (2017) Chlorine and fluorine partitioning between apatite and sediment melt at 2.5 GPa, 800 °C: A new experimentally derived thermodynamic model. Am Mineral 102:580–594. https://doi.org/10.2138/am-2017-5891

Linnen RL, Van Lichtervelde M, Cerny P (2012) Granitic pegmatites as sources of strategic metals. Elements 8(4):275–280. https://doi.org/10.2113/gselements.8.4.275

Liu YS, Hu ZC, Zong KQ, Gao CG, Gao S, Xu J, Chen HH (2010) Reappraisement and refinement of zircon U-Pb isotope and trace element analyses by LA-ICP-MS. Chin Sci Bull 55(15):1535–1546. https://doi.org/10.1007/s11434-010-3052-4

Liu XC, Matthew J, Kohn B, Wang JM, He SX, Wang RC, Liu ZC, Wu FY, Liu XC, Wang JG (2020) The mechanisms of fractional crystallization for the Himalayan leucogranites. Acta Petrol Sin 36(12):3551–3571 (**in Chinese with English abstract**)

Liu XC, Kohn MJ, Wang JM, He SX, Wang RC, Wu FY (2024) Formation of lithium-rich pegmatites *via* rapid crystallization and shearing–case study from the South Tibetan Detachment, Himalaya. Earth Planet Sci Lett 629:118598. https://doi.org/10.1016/j.epsl.2024.118598

London D (2014) A petrologic assessment of internal zonation in granitic pegmatites. Lithos 184:74–104. https://doi.org/10.1016/j.lithos.2013.10.025

London D (2018) Ore-forming processes within granitic pegmatites. Ore Geol Rev 101:349–383. https://doi.org/10.1016/j.oregeorev.2018.04.020

Mao M, Rukhlov AS, Rowins SM, Spence J, Coogan LA (2016) Apatite trace element compositions: a robust new tool for mineral exploration. Econ Geol 111(5):1187–1222. https://doi.org/10.2113/econgeo.111.5.1187

Mercer CN, Watts KE, Gross J (2020) Apatite trace element geochemistry and cathodoluminescent textures: a comparison between regional magmatism and the Pea Ridge IOAREE and Boss IOCG deposits, southeastern Missouri iron metallogenic province, USA. Ore Geol Rev 116:103129. https://doi.org/10.1016/j.oregeorev.2019.103129

Miles AJ, Graham CM, Hawkesworth CJ, Gillespie MR, Hinton RW, Bromiley GD (2014) Apatite: A new redox proxy for silicic magmas? Geochim Cosmochim Acta 132:101–119. https://doi.org/10.1016/j.gca.2014.01.040

O'Sullivan G, Chew D, Kenny G, Henrichs I, Mulligan D (2020) The trace element composition of apatite and its application to detrital provenance studies. Earth Sci Rev 201:103044. https://doi.org/10.1016/j.earscirev.2019.103044

Pan Y, Fleet ME (2002) Compositions of the apatite-group minerals: substitution mechanisms and controlling factors. Rev Mineral Geochem 48(1):13–49. https://doi.org/10.2138/rmg.2002.48.2

Pan LC, Hu RZ, Wang XS, Bi XW, Zhu JJ, Li CS (2016) Apatite trace element and halogen compositions as petrogenetic-metallogenic indicators: Examples from four granite plutons in the Sanjiang region SW China. Lithos 254-255:118–130. https://doi.org/10.1016/j.lithos.2016.03.010

Pan LC, Hu RZ, Oyebamiji A, Wu HY, Li JW, Li JX (2021) Contrasting magma compositions between Cu and Au mineralized granodiorite intrusions in the Tongling ore district in South China using apatite chemical composition and Sr-Nd isotopes. Am Mineral 106(12):1873–1889. https://doi.org/10.2138/am-2021-7497

Qin KZ, Zhao JX, He CT, Shi RZ (2021) Discovery of the Qiongjiagang giant lithium pegmatite deposit in Himalaya, Tibet, China. Acta Petrol Sin 37:3277–3286 (**in Chinese with English abstract**)

Qu P, Li NB, Niu HC, Shan Q, Weng Q, Zhao XC (2021) Difference in the nature of ore-forming magma between the Mesozoic porphyry

Cu-Mo and Mo deposits in NE China: records from apatite and zircon geochemistry. Ore Geol Rev 135:104218. https://doi.org/10.1016/j.oregeorev.2021.104218

Qu P, Yang WB, Niu HC, Li NB, Wu D (2022) Apatite fingerprints on the magmatic-hydrothermal evolution of the Daheishan giant porphyry Mo deposit, NE China. Geol Soc Am Bull 134(7–8):1863–1876. https://doi.org/10.1130/B36093.1

Rønsbo JG (1989) Coupled substitutions involving REEs and Na and Si in apatites in alkaline rocks fromthe IlÍmaussaq intrusion, South Greenland, and the petrological implications. Am Mineral 74:896–901

Rudnick RL, Gao S (2003) Composition of the continental crust. Treatise Geochem 3:659. https://doi.org/10.1016/B0-08-043751-6/03016-4

Searle MP, Cottle JM, Streule MJ, Waters DJ (2009) Crustal melt granites and migmatites along the Himalaya: melt source, segregation, transport and granite emplacement mechanisms. Earth Environ Sci Trans R Soc Edinb 100(1–2):219–233. https://doi.org/10.1017/s175569100901617x

Sha LK, Chappell BW (1999) Apatite chemical composition, determined by electron microprobe and laser-ablation inductively coupled plasma mass spectrometry, as a probe into granite petrogenesis. Geochim Cosmochim Acta 63(22):3861–3881. https://doi.org/10.1016/S0016-7037(99)00210-0

Shi RZ, Zhao JX, Romer RL, He CT, Qin KZ (2024) Zircon and apatite textures and compositions document fluid exsolution in highly evolved Li granite-pegmatite systems. Lithos 480:107667. https://doi.org/10.1016/j.lithos.2024.107667

Sun SS, McDonough WF (1989) Chemical and isotopic systematics of oceanic basalts: Implications for mantle composition and processes. Geol Soc Lond Spec Publ 42(1):313–345. https://doi.org/10.1144/GSL.SP.1989.042.01.19

Troch J, Huber C, Bachmann O (2022) The physical and chemical evolution of magmatic fluids in near-solidus silicic magma reservoirs: implications for the formation of pegmatites. Am Mineral 107(2):190–205. https://doi.org/10.2138/am-2021-7915

Wang M, Wang CY (2020) Crystal size distributions and trace element compositions of the fluorapatite from the Bijigou Fe–Ti oxide-bearing layered intrusion, central China: insights for the expulsion processes of interstitial liquid from crystal mush. J Petrol 61:1–17

Wang RC, Wu FY, Xie L, Liu XC, Wang JM, Yang L, Lai W, Liu C (2017) A preliminary study of rare-metal mineralization in the Himalayan leucogranite belts, South Tibet. Sci China Earth Sci 60(9):1655–1663. https://doi.org/10.1007/s11430-017-9075-8

Watson EB, Green TH (1981) Apatite/liquid partition coefficients for the rare earth elements and strontium. Earth Planet Sci Lett 56:405–421. https://doi.org/10.1016/0012-821X(81)90144-8

Webster JD, Piccoli PM (2015) Magmatic apatite: a powerful, yet deceptive, mineral. Elements 11(3):177–182. https://doi.org/10.2113/gselements.11.3.177

Williams-Jones AE, Migdisov AA, Samson IM (2012) Hydrothermal mobilisation of the rare earth elements—a tale of "Ceria" and "Yttria." Elements 8(5):355–360. https://doi.org/10.2113/gselements.8.5.355

Wu FY, Liu XC, Liu ZC, Wang RC, Xie L, Wang JM, Ji WQ, Yang L, Liu C, Khanal GP, He SX (2020) Highly fractionated Himalayan leucogranites and associated rare-metal mineralization. Lithos 352:105319. https://doi.org/10.1016/j.lithos.2019.105319

Wu WZ, Lang XH, Wang XH, Deng YL, Du LY, Wang YT, Jiang K, Zhan HY, Zhaxi PC, Fayek M (2024) Cathodoluminescence and geochemical characteristics of apatite: implications for mineral exploration in the Xiongcun district, Tibet. China Ore Geol Rev 164:105786. https://doi.org/10.1016/j.oregeorev.2023.105786

Wu HR, Yang H, Zhu YS, Santosh M, Chen ZY, Ji Z, Zhang ZC, Ge WC (2025) Zircon and apatite as tracers of physicochemical differences between barren and rare metal plutons in granite-pegmatite systems. Geol Soc Am Bull. https://doi.org/10.1130/b38016.1

Xing CM, Wang CY (2017) Cathodoluminescence images and trace element compositions of fluorapatite from the Hongge layered intrusion in SW China: a record of prolonged crystallization and overprinted fluid metasomatism. Am Mineral 102(7):1390–1401. https://doi.org/10.2138/am-2017-6028

Xu XW, Zhai MG, Hong T, Ma YC, Guo JH (2023) Migration-circulation processes and enrichment-mineralization mechanism of lithium-beryllium elements in the continental crust. Acta Petrol Sin 39(3):639–658 (**in Chinese with English abstract**)

Zhang XN, Pan JY, Lehmann B, Li JX, Yin S, Ouyang YP, Wu B, Fu JL, Zhang Y, Sun Y, Wan JJ, Liu T (2023) Diagnostic REE patterns of magmatic and hydrothermal apatite in the Zhuxi tungsten skarn deposit, China. J Geochem Explor 252:107271. https://doi.org/10.1016/j.gexplo.2023.107271

Zhao JX, He CT, Qin KZ, Shi RZ, Liu XC, Hu FY, Yu KL, Sun ZH (2021) Geochronology, source features and the characteristics of fractional crystallization in pegmatite at the Qiongjiagang giant pegmatite-type lithium deposit, Himalaya, Tibet. Acta Petrol Sin 37:3325–3347 (**in Chinese with English abstract**)